

1                    **Breaking the ice: Identifying hydraulically-forced crevassing**

2  
3 T.S. Hudson<sup>1\*</sup>, A.M. Brisbourne<sup>2</sup>, R.S. White<sup>3</sup>, JM. Kendall<sup>1</sup>, R. Arthern<sup>2</sup>, A.M. Smith<sup>2</sup>

4  
5 <sup>1</sup> *Department of Earth Sciences, University of Oxford, Oxford, UK*

6 <sup>2</sup> *British Antarctic Survey, Cambridge, UK*

7 <sup>3</sup> *Bullard Laboratories, University of Cambridge, Cambridge, UK*

8  
9 Corresponding author: Thomas S. Hudson (thomas.hudson@earth.ox.ac.uk)

10  
11 **Key Points:**

- 12        • We demonstrate a novel method for using crevasse icequake depths to discriminate  
13            between dry and hydrofracture driven surface crevassing
- 14        • Icequakes can be used to directly observe and elucidate the crevasse hydrofracture  
15            process
- 16        • Icequakes show tensile crack failure with opening volumes calculated from moment  
17            magnitudes

26 **Abstract**

27

28 Hydraulically-forced crevassing is thought to reduce the stability of ice shelves and ice  
29 sheets, affecting structural integrity and providing pathways for surface meltwater to the bed.  
30 It can cause ice shelves to collapse and ice sheets to accelerate into the ocean. However,  
31 direct observations of the hydraulically-forced crevassing process remain elusive. Here we  
32 report a new, novel method and observations that use icequakes to directly observe  
33 crevassing and determine the role of hydrofracture. Crevasse icequake depths from seismic  
34 observations are compared to a theoretically derived maximum-dry-crevasse-depth. We  
35 observe icequakes below this depth, suggesting hydrofracture. Furthermore, icequake source  
36 mechanisms provide insight into the fracture process, with predominantly opening cracks  
37 observed, which have opening volumes of tens to hundreds of cubic meters. Our method and  
38 findings provide a framework for studying a critical process, key for the stability of ice  
39 shelves and ice sheets, and hence rates of future sea-level rise.

40

41 **1 Introduction**

42

43 Hydraulically-forced surface crevassing, also referred to as hydrofracture, has the potential to  
44 significantly influence the stability of glaciers, ice sheets and ice shelves (Lai et al., 2020).  
45 On glaciers and ice sheets, hydraulically-forced crevassing provides a potential pathway for  
46 surface meltwater to reach and lubricate the bed (Das et al., 2008; Van Der Veen, 1998;  
47 Weertman, 1973), enhancing basal sliding of ice into the ocean (Rignot & Kanagaratnam,  
48 2006), accelerating sea-level rise. Hydraulically-forced surface crevassing on ice shelves can  
49 result in catastrophic failure, with melt ponds promoting fracture that can lead to the collapse  
50 of the ice shelf (Hughes, 1983; Mcgrath et al., 2012; T. Scambos et al., 2003; T. A. Scambos

51 et al., 2000). Following ice shelf collapse, land-based glaciers can accelerate into the ocean,  
52 since the buttressing provided by the ice shelf no longer exists, again contributing to sea-level  
53 rise. Understanding the fundamental mechanism of hydraulically-forced surface crevassing is  
54 therefore a particularly timely topic within glaciology.

55

56 Here, we present icequake observations from Skeidararjökull, an outlet glacier of the  
57 Vatnajökull Ice Cap, Iceland. This glacier is an ideal environment for studying potential  
58 hydraulically-forced crevassing due to the high levels of surface melt present. Previous  
59 studies have used icequakes to infer hydraulically-forced crevassing using auxiliary  
60 information, such as glacier speed up (Helmstetter et al., 2015), or the presence of meltwater  
61 (Carmichael et al., 2012, 2015). Others have used seismicity to show that crevassing exhibits  
62 tensile faulting (Mikesell et al., 2012; Neave & Savage, 1970; Roux et al., 2010; Walter et al.,  
63 2009). We first present a novel method for attributing an icequake to either dry or  
64 hydraulically-forced crevassing, providing evidence that the icequakes we observe are likely  
65 induced by hydrofracture. We then use icequake source mechanisms to confirm the  
66 crevassing stress release mechanism. Our results provide for the first time direct evidence of  
67 hydrofracture, offering insights into this previously elusive process.

68

## 69 **2 Methods**

70 Here, we briefly describe the methods for detecting and locating the seismicity, as well as an  
71 overview of how the source mechanism inversions are undertaken and moment magnitudes,  
72  $M_w$ , are calculated. Two additional fundamental methods used in this study are obtaining  
73 crevasse icequake depths from P-to-Rayleigh-wave amplitude ratios and the calculation of a  
74 theoretical maximum-dry-crevasse-depth, based on the rheology of ice. These methods and

75 theory are too complex to adequately describe in the main text, so we instead describe them  
76 in the Supplementary Information (Supplementary Text S1 and S2, respectively).

77

## 78 **2.1 Seismicity**

79 The seismicity presented in this study is detected using QuakeMigrate (Hudson et al., 2019;  
80 Smith et al., 2020), with the method and overall catalogue of icequakes detailed by Hudson et  
81 al (2019). We relocate the detected earthquakes using NonLinLoc (Lomax & Virieux, 2000)  
82 to obtain more accurate epicentral locations. For the subset of events presented in detail in  
83 Figure 1 and 2, we manually pick P and S phase arrivals before relocation. The crevassing  
84 icequake hypocentral depths for the selected events are obtained using P-to-Rayleigh-wave  
85 amplitude ratios, with the associated method details given in the Supplementary Information  
86 (Supplementary Text S1).

87

88 The icequake source mechanisms are obtained by performing a Bayesian full waveform  
89 source inversion using an identical approach to a method detailed by Hudson et al (n.d.).  
90 Only P-wave phases are used since the horizontal components are generally too noisy to use,  
91 due to the instruments melting out of the glacier. Theoretically, S and surface waves could  
92 also be used to constrain the inversion, but the amplitudes of any S arrivals are generally  
93 close to the noise levels and we have low confidence in our ability to model the polarity of  
94 dispersive surface waves sufficiently accurately for a moment tensor inversion, given the  
95 depth dependent velocity structure of the firn layer at the site. We use a finite difference  
96 scheme to model the Green's functions used to produce the synthetic seismograms in the  
97 inversion. The depth of the source, a critical parameter affecting the source inversion, is  
98 constrained using P-to-Rayleigh amplitude ratios.

99

100 The moment magnitude,  $M_w$ , of the icequakes is calculated using a spectral method(Stork et  
 101 al., 2014). The spectrum of the icequake is calculated by performing multi-taper spectral  
 102 estimation(Krischer, 2016; Prieto et al., 2009) in order to find the long period spectral level  
 103 and hence the seismic moment release,  $M_0$ .  $M_w$  can then be calculated from (Hanks &  
 104 Kanamori, 1979),

$$105 \quad M_w = \frac{2}{3} \log_{10}(M_0) - 6.0. \quad (1)$$

106 If one assumes that all the moment release for a given icequake is released via tensile failure,  
 107 then the opening of a crack,  $\Delta V$ , can be calculated from,

$$108 \quad \Delta V = \frac{M_0}{\sigma_T} \quad (2)$$

109 where  $\sigma_T$  is the tensile strength of the ice, taken to be 1.5 MPa (Podolskiy & Walter, 2016) in  
 110 this study.

111

## 112 **3 Results**

### 113 **3.1 Evidence for dry fracture vs. hydrofracture from crevasse depth**

114

115 As a crevasse propagates, the ice fractures, releasing seismic energy as icequakes. Crevasses  
 116 ordinarily only propagate to a certain depth within the ice column, where the tensile stress  
 117 field causing crevasse opening is compensated by the ice overburden pressure acting to close  
 118 the crevasse. We refer to this depth limit as the maximum-dry-crevasse-depth,  $d^*$ . However,  
 119 if the crevasse contains sufficient water, the additional pressure of this water column can  
 120 overcome the ice overburden pressure and induce hydrofracture, allowing the crevasse to  
 121 propagate to greater depths (Nick et al., 2010; Van Der Veen, 1998). Therefore, if the  
 122 observed depth of a crevasse icequake is greater than  $d^*$ , then one can infer that the icequake  
 123 is induced by hydrofracture. This is the fundamental premise of this study.

124

125 However, obtaining sufficiently accurate icequake hypocentral depths for comparison to  $d^*$  is  
126 non-trivial. Seismometer networks are inherently poor at constraining the depth of an  
127 earthquake using traditional body wave methods if the source-receiver epicentral distance is  
128 much greater than the source depth. This is generally the case in our study. Since the depth of  
129 an icequake is critical evidence for or against hydrofracture, a more accurate method is  
130 required for constraining hypocentral depth. We use surface-wave information in the form of  
131 P-wave to Rayleigh-wave amplitude ratios to constrain hypocentral depth (Heyburn et al.,  
132 2013; Jia et al., 2017; Stein & Wiens, 1986; Tsai & Aki, 1970). Figure 1a shows finite-  
133 difference full-waveform modelling results (Larsen et al., 2001) and observations of P to  
134 Rayleigh amplitude ratios, plotted against epicentral distance for a range of crevasse depths.  
135 The observed amplitude ratios are compared to the model results to calculate the crevassing  
136 depths. We independently verify these crevasse depths using P-S delay-times from receivers  
137 close to the source epicentre where possible (See Supplementary Figure S1), giving us  
138 confidence that the amplitude ratios provide a sufficiently accurate estimation of icequake  
139 depth.

140

141 The crevassing depths constrained by the observations in Figure 1 can then be compared to  
142 the maximum-dry-crevasse-depths, shown in Figure 2b, derived from the surface velocity  
143 field shown in Figure 2a. Figure 2c shows the epicentral locations of the near surface  
144 seismicity, with the grey scatter points showing the automatically detected icequakes(Thomas  
145 S Hudson et al., 2019) and the coloured scatter points showing a subset of manually relocated  
146 events. The majority of this subset of icequakes are located below  $d^*$  (solid red line, Figure  
147 2d), on average 7.4 m deeper, from which we infer that they may be induced by  
148 hydrofracture.

149

150 One potential limitation of using the source depth to discriminate between hydrofracture and  
151 dry fracture is that we do not account for dynamic rupture, whereby during the rupture, a  
152 crack may propagate deeper than the prevailing stress field otherwise allows, initiated by  
153 fracture tip instability (Buehler & Gao, 2006). For the purposes of this study we treat each  
154 icequake as an instantaneous point source, therefore neglecting dynamic rupture. Although  
155 this assumption is does not fully describe the physics of the source, we deem it appropriate  
156 here because of the distinct, high-frequency and short-duration phase arrivals observed.

157

158 Given that the events are predominantly deeper than  $d^*$ , we suggest that the majority of these  
159 events are likely caused by hydraulically-forced crevassing. In any case, the methodologies  
160 developed here, which constrain icequake depth from amplitude ratios and use this source  
161 depth to discriminate hydrofracture, are important developments for studying hydrofracture-  
162 induced crevassing.

163

164

### 165 **3.2 Crevassing source mechanisms**

166

167 Moment tensor inversions constrain whether icequake source mechanisms include explosive,  
168 implosive, crack, or shear components. Icequake magnitudes then give the volume of  
169 opening, or fault area and displacement, depending upon the icequake source mechanism.

170

171 Figure 2c shows the P-wave-constrained moment tensor inversion results for the subset of  
172 icequakes for which sufficiently accurate depths have been obtained. The inversion results for  
173 two of these icequakes are presented in more detail in Figure 3. For both icequakes, the

174 waveform polarities are all correctly inverted for. Lune plots (Tape & Tape, 2012) in Figure  
175 3b and Figure 3d indicate that the most likely source mechanisms for the two icequakes are a  
176 closing and an opening crack, respectively, with a negligible shear component in both cases.  
177 Such crack mechanisms are the mode of failure one might expect from either dry or  
178 hydraulically-forced crevassing. However, after considering the Probability Density Function  
179 (PDF) of the inversion solutions for the closing crack icequake in Figure 3b, an opening  
180 crack mechanism cannot be eliminated. This ambiguity is due to station geometry on the  
181 focal sphere. In any case, an opening or closing crack of a specific orientation is required to  
182 represent the observations adequately, as inferred from previous seismic observations  
183 (Mikesell et al., 2012; Neave & Savage, 1970; Roux et al., 2010; Walter et al., 2009).

184

185 All icequake crack orientations in Figure 2c agree with the principal stress directions  
186 calculated from the observed surface velocities, as shown by the orange vectors in Figure 2c.  
187 This confirms interpretations in previous studies (Garcia et al., 2019; Harper et al., 1998).  
188 The apparent closing crack observation for the icequake at 64.327° N, 17.21° W may be  
189 supported by the presence of tensile stresses in both principal stress directions. In such a  
190 stress regime, a closing crack may be valid, effectively exhibiting two-dimensional necking  
191 in the surface-parallel plane.

192

193 The moment magnitude of the crevassing icequakes range from -0.4 to -0.9, calculated using  
194 a spectral method (Stork et al., 2014). If we approximate all the failure as tensile, then for a  
195 tensile strength of ice of 1.5 MPa (Podolskiy & Walter, 2016), the volume associated with  
196 crack opening or closing is of the order of 30  $m^3$  to 150  $m^3$ .

197

198 We propose several possible mechanisms for generating seismicity below the maximum-dry-  
199 crevasse-depth. These interpretations are summarised in Figure 4. The mechanisms are: (1)  
200 new cracks opening when the combined deviatoric near-surface stress field and hydrostatic  
201 pressure are sufficient to overcome the ice overburden pressure and tensile strength of the  
202 ice; (2) pre-existing cracks that have closed reopening due to a sufficient head of water in the  
203 crevasse; (3) opened pre-existing cracks reclosing as the water is evacuated from the fracture,  
204 due to a preferential pressure gradient below the fracture.

205

206 For mechanisms 2 and 3, the crevasse must have propagated to that depth via mechanism 1,  
207 therefore suggesting that at least some of the icequakes we observe are likely to be new ice  
208 fracture. We observe principal tensile stress amplitudes of greater than 200 kPa (see Figure  
209 S2), more than sufficient to overcome an ice tensile strength of  $\sim 100$  kPa (Paterson, 1994).

210 Mechanism 2 is similar to mechanism 1, except requiring a lower hydrostatic pressure to  
211 induce crack opening, and is possible if crevasses have formed upstream and subsequently  
212 been closed by principal compressive stresses perpendicular to the crevasse. Such  
213 refracturing is proposed in scenarios where there are insufficient volumes of surface  
214 meltwater to immediately establish a permanent bed connection (Boon & Sharp, 2003).

215 Mechanism 3 is presented more tentatively, partly due to the potential ambiguity of the  
216 closing-crack source mechanism (see Figure 3a), but also because these crevasses would have  
217 to close over sufficiently short time scales to generate the  $\sim 100$  Hz source frequencies  
218 observed in the P-wave spectra. While ice can suddenly fail or reopen a crack over such a  
219 short duration, a possible source of driving stresses or pressures required to close cracks this  
220 quickly is less conceivable. A crack at greater depth could reopen, evacuating water from  
221 above, but envisaging a sufficiently localised stress field is difficult. Alternatively, water may  
222 travel through an opening, pre-existing crack sufficiently quickly that the crack then

223 immediately closes, although the magnitude of closing would have to dominate over opening  
224 to explain a closing-crack observation. In summary, we therefore confidently present  
225 mechanisms 1 and 2, but suggest that mechanism 3 is unlikely.

226

227 One question that arises is why we do not observe seismicity via mechanism 1 or 2 occurring  
228 all the way to the glacier bed, as is proposed in various studies (Boon & Sharp, 2003;  
229 Carmichael et al., 2012; Colgan et al., 2016; Van Der Veen, 1998; Weertman, 1973). A  
230 reason could be that as such fractures penetrate deeper into the glacier, the energy will be  
231 more attenuated, fall below background noise levels and not be detected. Alternatively, the  
232 crevasses at Skeidararjökull might never reach the bed.

233

234 These results emphasise the potential information that icequakes hold for elucidating the  
235 physics of glacier hydrofracture. Here, we only use P-waves to constrain the mechanisms, but  
236 if one had a more comprehensive dataset with a greater number of receivers and higher SNR,  
237 then it may be possible to constrain the source mechanism better. Furthermore, if one were to  
238 invert for a dynamic rupture model of finite length, rather than the instantaneous point source  
239 that we assume here, then one might gain additional insight into the physics governing  
240 hydrofracture in ice. Another approach to learn more about the hydrofracture process could  
241 be to compare observations such as ours to theoretical models of crevasse vibrational modes  
242 to infer crevasse geometry (Lipovsky & Dunham, 2015), or even models of supraglacial lake  
243 drainage (Jones et al., 2013).

244

245

246

247

248 **4 Implications for ice sheet and ice shelf stability**

249

250 Our findings provide a method for observing hydrofracture at icesheets such as the Greenland  
251 Ice Sheet, where although it has been shown that meltwater can drain from the surface to the  
252 bed (Das et al., 2008), the mechanism and pathway has not been imaged previously. Calving  
253 at the ocean termini of outlet glaciers of the Greenland Ice Sheet could also be enhanced by  
254 hydrofracture. Increased calving could be facilitated by precipitation increasing the  
255 hydrostatic pressure of water-filled crevasses (O’Neel et al., 2003), or by damage to the  
256 upstream ice (Krug et al., 2014), with the depth of this damage through the ice column  
257 dependent upon the depth of the crevasses, which we infer here to be controlled by the glacier  
258 stress state and hydrofracture. Our method could provide observations of the depth of such  
259 damage. The above mechanisms are also hypothesised to be important factors that could  
260 accelerate the collapse of the West Antarctic Ice Sheet and cause significant retreat of the  
261 East Antarctic Ice Sheet (Pollard et al., 2015).

262

263 Some ice shelves exhibit surface melt ponds before undergoing disintegration, whereas others  
264 have similar melt ponds but remain intact (Scambos et al., 2000). Crevassing icequakes could  
265 provide insight into whether hydrofracture is occurring unnoticed at these apparently stable  
266 ice shelves, potentially leading to sudden future catastrophic collapse, or whether  
267 hydrofracture is physically suppressed by another mechanism that affects either the stress  
268 regime or the fracture toughness of the ice.

269

270 In conclusion, understanding the stability of ice sheets and ice shelves is important for sea-  
271 level-rise projections (Vaughan et al., 2013). Hydrofracture induced crevassing is an  
272 important mechanism that, at least to some extent, controls the stability of such ice bodies.

273 The methodology and findings we present provide a means of attributing crevassing  
274 icequakes to hydrofracture. We show that such icequakes can then be used as an  
275 observational basis for studying the physical mechanisms associated with hydrofracture  
276 induced crevassing.

277

## 278 **Acknowledgements**

279

280 T. Hudson was funded by a Natural Environment Research Council (NERC) Studentship  
281 (NE/L002507/1) for the majority of this work. We thank Antony Butcher for useful  
282 conversations regarding the waveform propagation modelling. We thank Hunter Philson,  
283 University of Iceland and the Icelandic Glaciological Society for fieldwork support, without  
284 which this study would not have been possible. We also thank Finnur Pálsson and the  
285 glaciology group at the University of Iceland for the radar bed topography data, and Robert  
286 Green for pre-processing the data. Seismometers were borrowed from SeisUK (Geophysical  
287 Equipment Facility loan number 1022) and NERC British Antarctic Survey. Seismic data will  
288 be made available on IRIS. Software used includes: QuakeMigrate  
289 (<https://github.com/QuakeMigrate>); NonLinLoc (<http://alomax.free.fr/nlloc/>); SeisSrcInv  
290 (<https://github.com/TomSHudson/SeisSrcInv>) for the moment tensor inversion;  
291 SeisSrcMoment (<https://github.com/TomSHudson/SeisSrcMoment>) for the moment  
292 magnitude calculation.

293

294

295

296

297

298 **References**

299

300 Björnsson, H. (2017). *The Glaciers of Iceland*. Paris: Atlantis Press.

301 <https://doi.org/10.2991/978-94-6239-207-6>

302 Boon, S., & Sharp, M. (2003). The role of hydrologically-driven ice fracture in drainage  
303 system evolution on an Arctic glacier. *Geophysical Research Letters*, *30*(18), 3–6.

304 <https://doi.org/10.1029/2003GL018034>

305 Buehler, M. J., & Gao, H. (2006). Dynamical fracture instabilities due to local hyperelasticity  
306 at crack tips. *Nature*, *439*(7074), 307–310. <https://doi.org/10.1038/nature04408>

307 Carmichael, J. D., Pettit, E. C., Hoffman, M., Fountain, A., & Hallet, B. (2012). Seismic  
308 multiplet response triggered by melt at Blood Falls, Taylor Glacier, Antarctica. *Journal*  
309 *of Geophysical Research: Earth Surface*, *117*(3), 1–16.

310 <https://doi.org/10.1029/2011JF002221>

311 Carmichael, J. D., Joughin, I., Behn, M. D., Das, S., King, M. A., Stevens, L., & Lizarralde,  
312 D. (2015). Seismicity on the western Greenland Ice Sheet: Surface fracture in the  
313 vicinity of active moulins. *Journal of Geophysical Research : Earth Surface*, *120*, 1082–  
314 1106. <https://doi.org/10.1002/2014JF003398>.Received

315 Colgan, W., Rajaram, H., Abdalati, W., Mccutchan, C., Mottram, R., Moussavi, M. S., &  
316 Grigsby, S. (2016). Glacier crevasses: Observations, models, and mass balance  
317 implications. *Reviews of Geophysics*, *54*, 119–161.

318 <https://doi.org/10.1002/2015RG000504>

319 Das, S. B., Joughin, I., Behn, M. D., Howat, I. M., King, M. A., Lizarralde, D., & Bhatia, M.  
320 P. (2008). Fracture propagation to the base of the Greenland Ice Sheet during  
321 supraglacial lake drainage. *Science*, *320*, 778–782.

322 Garcia, L., Luttrell, K., Kilb, D., & Walter, F. (2019). Joint geodetic and seismic analysis of

- 323 surface crevassing near a seasonal glacier-dammed lake at Gornergletscher, Switzerland.  
324 *Annals of Glaciology*, 1–13. <https://doi.org/10.1017/aog.2018.32>
- 325 Gudmundsson, M. T. (1989). The Grimsvotn Caldera, Vatnajokull: Subglacial Topography  
326 and Structure of Caldera Infill. *Jokull*, 39, 3–7.
- 327 Hanks, T. C., & Kanamori, H. (1979). A moment magnitude scale. *Journal of Geophysical*  
328 *Research*, 84(B5), 2348. <https://doi.org/10.1029/JB084iB05p02348>
- 329 Harper, J. T., Humphrey, N. F., & Pfeffer, W. T. (1998). Crevasse patterns and the strain-rate  
330 tensor : a high-resolution comparison. *Journal of Glaciology*, 44(146).
- 331 Helmstetter, A., Nicolas, B., Comon, P., & Gay, M. (2015). Basal icequakes recorded  
332 beneath an alpine glacier (Glacier d'Argentière, Mont Blanc, France): Evidence for  
333 stick-slip motion? *Journal of Geophysical Research: Earth Surface*, 120(3), 379–401.  
334 <https://doi.org/10.1002/2014JF003288>
- 335 Heyburn, R., Selby, N. D., & Fox, B. (2013). Estimating earthquake source depths by  
336 combining surface wave amplitude spectra and teleseismic depth phase observations.  
337 *Geophysical Journal International*, 194, 1000–1010. <https://doi.org/10.1093/gji/ggt140>
- 338 Hudson, T S, Brisbourne, A. M., Walter, F., Graff, D., & White, R. S. (n.d.). Icequake source  
339 mechanisms for studying glacial sliding. *Journal of Geophysical Research : Earth*  
340 *Surface (in Review)*. <https://doi.org/10.1002/essoar.10502610.1>
- 341 Hudson, Thomas S, Smith, J., Brisbourne, A., & White, R. (2019). Automated detection of  
342 basal icequakes and discrimination from surface crevassing. *Annals of Glaciology*,  
343 60(79), 1–11.
- 344 Hughes, B. T. (1983). On the disintegration of ice shelves: The role of fracture. *Journal of*  
345 *Glaciology*, 29(101), 98–117.
- 346 Jia, Z., Ni, S., Chu, R., & Zhan, Z. (2017). Joint inversion for earthquake depths using local  
347 waveforms and amplitude spectra of Rayleigh waves. *Pure and Applied Geophysics*,

- 348 174, 261–277. <https://doi.org/10.1007/s00024-016-1373-1>
- 349 Jones, G. A., Kulessa, B., Doyle, S. H., Dow, C. F., & Hubbard, A. (2013). An automated  
350 approach to the location of icequakes using seismic waveform amplitudes. *Annals of*  
351 *Glaciology*, 54(64), 1–9. <https://doi.org/10.3189/2013AoG64A074>
- 352 Krischer, L. (2016). mtspec Python wrappers 0.3.2. *Zenodo*.  
353 <https://doi.org/10.5281/zenodo.321789>
- 354 Krug, J., Weiss, J., Gagliardini, O., & Durand, G. (2014). Combining damage and fracture  
355 mechanics to model calving. *The Cryosphere*, 8, 2101–2117. [https://doi.org/10.5194/tc-](https://doi.org/10.5194/tc-8-2101-2014)  
356 8-2101-2014
- 357 Lai, C., Kingslake, J., Wearing, M. G., Chen, P. C., Gentine, P., Li, H., et al. (2020).  
358 Vulnerability of Antarctica’s ice shelves to meltwater-driven fracture. *Nature*,  
359 584(7822), 574–578. <https://doi.org/10.1038/s41586-020-2627-8>
- 360 Larsen, S., Wiley, R., Roberts, P., & House, L. (2001). *Next-generation numerical modeling:*  
361 *incorporating elasticity, anisotropy and attenuation. Los Alamos National Laboratory*  
362 (Vol. LA-UR-01-1).
- 363 Lipovsky, B. P., & Dunham, E. M. (2015). Vibrational modes of hydraulic fractures:  
364 Inference of fracture geometry from resonant frequencies and attenuation. *Journal of*  
365 *Geophysical Research: Solid Earth*, 120(2), 1080–1107.  
366 <https://doi.org/10.1002/2014JB011286>
- 367 Lomax, A., & Virieux, J. (2000). Probabilistic earthquake location in 3D and layered models.  
368 *Advances in Seismic Event Location, Volume 18 of the Series Modern Approaches in*  
369 *Geophysics*, 101–134.
- 370 Mcgrath, D., Steffen, K., Scambos, T., Rajaram, H., Casassa, G., Luis, J., & Lagos, R.  
371 (2012). Basal crevasses and associated surface crevassing on the Larsen C ice shelf ,  
372 Antarctica , and their role in ice-shelf instability. *Annals of Glaciology*, 53(60), 10–18.

- 373 <https://doi.org/10.3189/2012AoG60A005>
- 374 Mikesell, T. D., Van Wijk, K., Haney, M. M., Bradford, J. H., Marshall, H. P., & Harper, J.  
375 T. (2012). Monitoring glacier surface seismicity in time and space using Rayleigh  
376 waves. *Journal of Geophysical Research: Earth Surface*, *117*(2), 1–12.  
377 <https://doi.org/10.1029/2011JF002259>
- 378 Neave, K. G., & Savage, J. C. (1970). Icequakes on the Athabasca Glacier. *Journal of*  
379 *Geophysical Research*, *75*(8), 1351–1362.
- 380 Nick, F. M., Van Der Veen, C. J., Vieli, A., & Benn, D. I. (2010). A physically based calving  
381 model applied to marine outlet glaciers and implications for the glacier dynamics.  
382 *Journal of Glaciology*, *56*(199), 781–794.
- 383 O’Neel, S., Echelmeyer, K. A., & Motyka, R. J. (2003). Short-term variations in calving of a  
384 tidewater glacier: LeConte Glacier, Alaska, U.S.A. *Journal of Glaciology*, *49*(167),  
385 587–598.
- 386 Paterson, W. S. B. (1994). *The Physics of Glaciers* (3rd Editio). Oxford: Butterworth-  
387 Heinemann.
- 388 Podolskiy, E. A., & Walter, F. (2016). Cryoseismology. *Reviews of Geophysics*, *54*, 1–51.  
389 <https://doi.org/10.1002/2016RG000526>
- 390 Pollard, D., DeConto, R. M., & Alley, R. B. (2015). Potential Antarctic Ice Sheet retreat  
391 driven by hydrofracturing and ice cliff failure. *Earth and Planetary Science Letters*, *412*,  
392 112–121. <https://doi.org/10.1016/j.epsl.2014.12.035>
- 393 Prieto, G. A., Parker, R. L., & Vernon, F. L. (2009). A Fortran 90 library for multitaper  
394 spectrum analysis. *Computers and Geosciences*, *35*(8), 1701–1710.  
395 <https://doi.org/10.1016/j.cageo.2008.06.007>
- 396 Rignot, E., & Kanagaratnam, P. (2006). Changes in the Velocity Structure of the Greenland  
397 Ice Sheet. *Science*, *311*, 986–991. <https://doi.org/10.1126/science.1121381>

- 398 Roux, P. F., Walter, F., Riesen, P., Sugiyama, S., & Funk, M. (2010). Observation of surface  
399 seismic activity changes of an Alpine glacier during a glacier dammed lake outburst.  
400 *Journal of Geophysical Research*, *115*, 1–13. <https://doi.org/10.1029/2009JF001535>
- 401 Scambos, T., Hulbe, C., & Fahnestock, M. (2003). Climate-induced ice shelf disintegration in  
402 the Antarctic Peninsula. *Antarctic Peninsula Climate Variability, Antarctic Research*  
403 *Series*, *79*, 79–92.
- 404 Scambos, T. A., Hulbe, C., Fahnestock, M., & Bohlander, J. (2000). The link between  
405 climate warming and break-up of ice shelves in the Antarctic Peninsula. *Journal of*  
406 *Glaciology*, *46*(1996).
- 407 Smith, J. D., White, R. S., Avouac, J.-P., & Bourne, S. (2020). Probabilistic earthquake  
408 locations of induced seismicity in the Groningen region, the Netherlands. *Geophysical*  
409 *Journal International*, *222*(1), 507–516. <https://doi.org/10.1093/gji/ggaa179>
- 410 Stein, S., & Wiens, D. A. (1986). Depth determination for shallow teleseismic earthquakes:  
411 Methods and results. *Reviews of Geophysics*, *24*(4), 806–832.
- 412 Stork, A. L., Verdon, J. P., & Kendall, J. M. (2014). The robustness of seismic moment and  
413 magnitudes estimated using spectral analysis. *Geophysical Prospecting*, *62*(4), 862–878.  
414 <https://doi.org/10.1111/1365-2478.12134>
- 415 Tape, W., & Tape, C. (2012). A geometric comparison of source-type plots for moment  
416 tensors. *Geophysical Journal International*, *190*(1), 499–510.  
417 <https://doi.org/10.1111/j.1365-246X.2012.05490.x>
- 418 Tsai, Y., & Aki, K. (1970). Precise focal depth determination from amplitude spectra of  
419 surface waves. *Journal of Geophysical Research*, *75*(29), 5729–5743.
- 420 Vaughan, D. ., Comiso, J. C., Allison, I., Carrasco, J., Kaser, G., Kwok, R., et al. (2013).  
421 *Chapter 4: Observations: Cryosphere. Climate Change 2013 the Physical Science*  
422 *Basis: Working Group I Contribution to the Fifth Assessment Report of the*

423 *Intergovernmental Panel on Climate Change*. Cambridge University Press, Cambridge,  
424 United Kingdom and New York, NY, USA.

425 <https://doi.org/10.1017/CBO9781107415324.012>

426 Van Der Veen, C. J. (1998). Fracture mechanics approach to penetration of surface crevasses  
427 on glaciers. *Cold Regions Science and Technology*, 27(1), 31–47.

428 [https://doi.org/10.1016/S0165-232X\(97\)00022-0](https://doi.org/10.1016/S0165-232X(97)00022-0)

429 Walter, F., Clinton, J. F., Deichmann, N., Dreger, D. S., Minson, S. E., & Funk, M. (2009).

430 Moment tensor inversions of icequakes on Gornergletscher, Switzerland. *Bulletin of the*  
431 *Seismological Society of America*, 99(2), 852–870. <https://doi.org/10.1785/0120080110>

432 Weertman, J. (1973). Can a water-filled crevasse reach the bottom surface of a glacier. *IASH*  
433 *Publ 95*, 139–145.

434

435

436

437

438

439

440

441

442

443

444

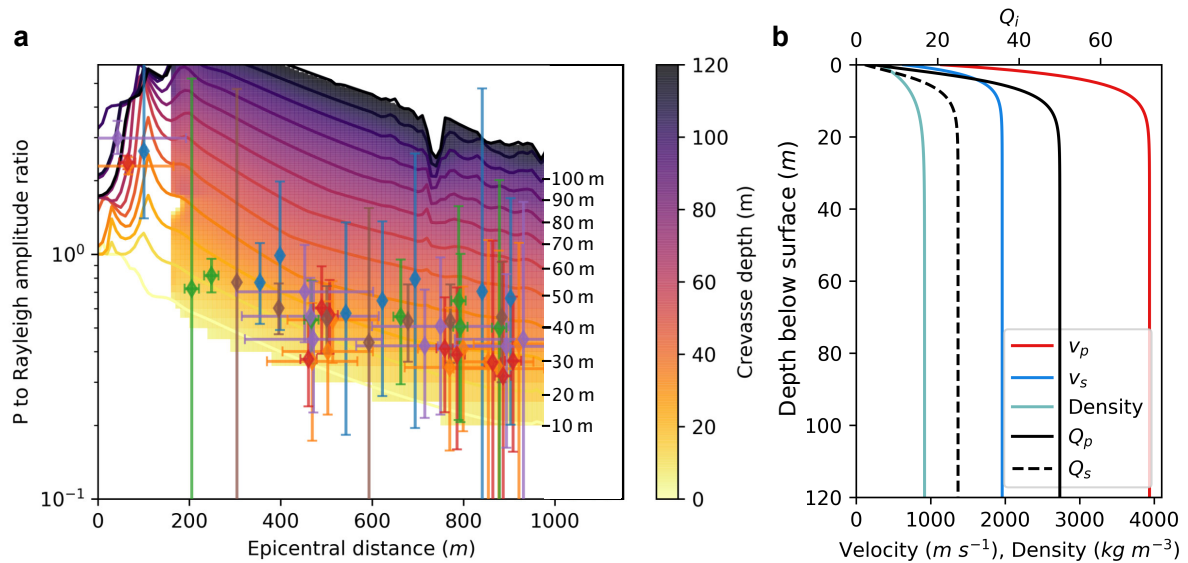
445

446

447

448 **Figures**

449

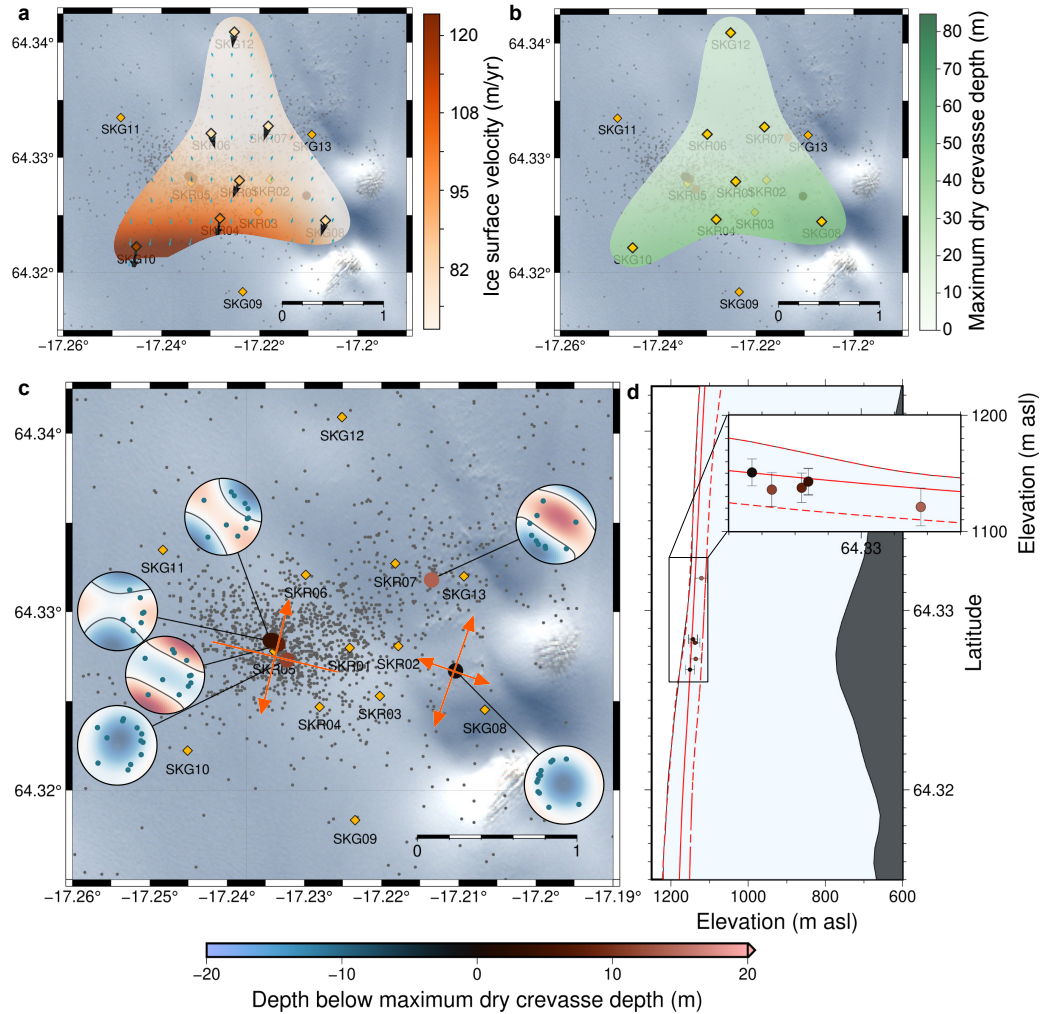


450

451 *Figure 1 – Obtaining depth for crevassing icequakes. a) Plot of P-to-Rayleigh-wave*  
 452 *amplitude ratio with epicentral distance from the source. Observed P-to-Rayleigh amplitudes*  
 453 *for the icequakes presented in Figure 2 are plotted (various coloured scatter points). P-to-*  
 454 *Rayleigh amplitudes for modelled crevassing icequakes with source depths from 10 to 120 m*  
 455 *below surface are indicated by the solid lines, with the 2D interpolated field plotted at*  
 456 *epicentral distances greater than 180 m. b) The velocity model used for the modelled*  
 457 *crevassing icequakes(Gudmundsson, 1989).*

458

459



460

461 *Figure 2 – Summary of crevasse icequake observations. a) The horizontal surface velocity*  
 462 *field at the site, derived using GPS data from the highlighted stations. b) The maximum-dry-*  
 463 *crevasse-depth,  $d^*$ , calculated using the velocity field in (a). Uncertainty in these fields are*  
 464 *given in Figure S2. c) Map of crevasse icequake locations. Grey scatter points are all the*  
 465 *crevasse icequakes detected during the period 19<sup>th</sup> to 29<sup>th</sup> June 2014. The icequakes studied*  
 466 *in more detail, with derived depths using the P-to-Rayleigh amplitude method are plotted as*  
 467 *larger scatter points, coloured by depth below the maximum dry crevasse depth. Upper*  
 468 *hemisphere moment tensors for these icequakes are also shown. Principal stress vectors*  
 469 *derived from the velocity field in (a) are shown in orange. Seismometer and geophone*  
 470 *locations are shown by the yellow diamonds. Satellite image is from the European Space*

471 *Agency. d) Plot of the crevassing events in (c) with depth vs. latitude projected onto a N-S*  
472 *transect at 17.225° W. The solid and dashed red lines indicate the maximum dry crevasse*  
473 *depth and the associated uncertainty, respectively. The bed topography is derived from*  
474 *ground-penetrating radar(Björnsson, 2017).*

475

476

477

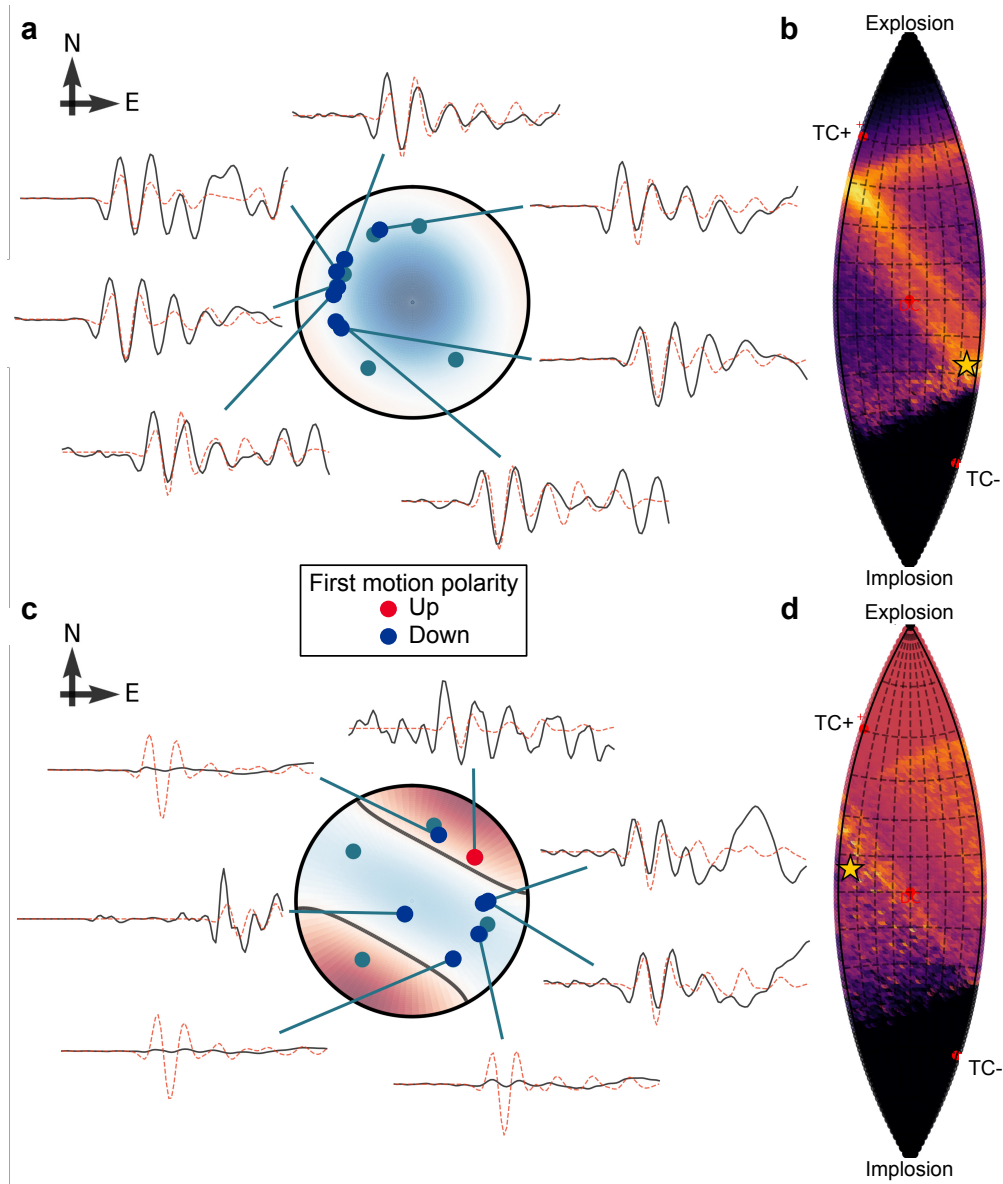
478

479

480

481

482



483

484 *Figure 3 – Examples of upper hemisphere crevasse icequake source mechanisms for two of*

485 *the events in Figure 2. The source mechanisms are constrained only by P-wave phases. a)*

486 *Source mechanism for a closing-crack crevasse icequake. Black waveforms are observed*

487 *data, red dashed waveforms are the most likely inversion model result. b) Lune plot (Tape*

488 *and Tape (2012)) associated with the event in (a), showing the PDF of the full waveform*

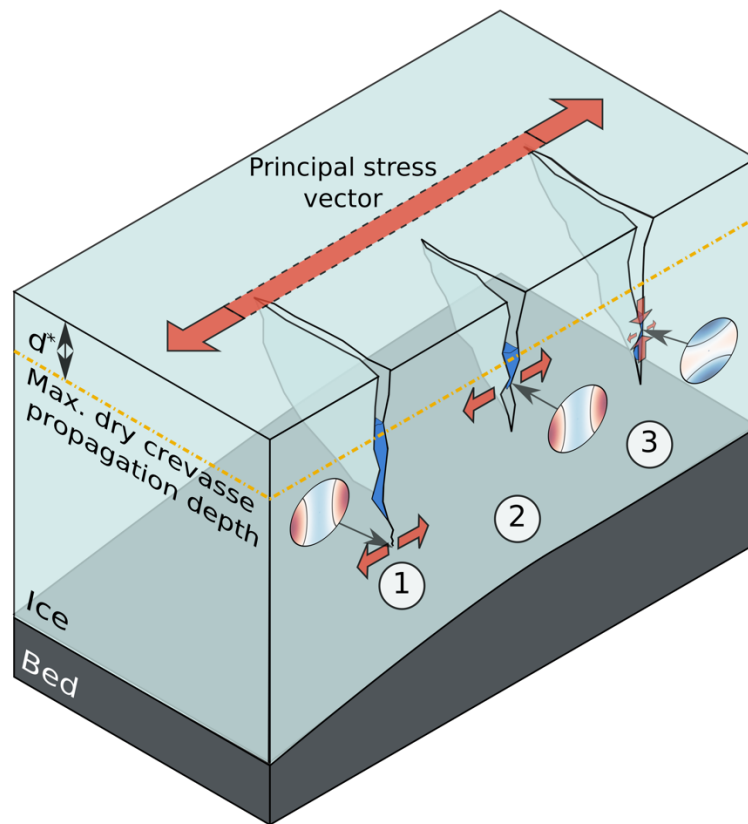
489 *inversion result, indicating the most likely source type. Brighter colours indicate higher*

490 *probability. c) and d) Same as (a) and (b) except for an opening-crack crevasse icequake.*

491

492

493



494

495 *Figure 4 – Interpretation of the possible crevasse failure mechanisms observed. (1) A new*  
 496 *opening-crack hydrofracture through previously undamaged ice. (2) An opening-crack*  
 497 *hydrofracture of a pre-existing crack. (3) Closing of a pre-existing crack due to the*  
 498 *evacuation of water from the crack. Hypothetical source mechanisms are shown for each*  
 499 *case.*

500

501